

A multi-year analysis of aerosol properties using the calibrated multi-wavelength polarisation lidar in Măgurele

V. NICOLAE¹, L. BELEGANTE^{1*}, J. VASILESCU¹, A. NEMUC¹, F. TOANCA¹, O. G. TUDOSE², C. RADU¹, D. NICOLAE¹

¹National Institute of Research and Development for Optoelectronics - INOE 2000, Remote Sensing Department, 409 Atomistilor street, Măgurele, PO Box MG-05, Măgurele, 077125, Romania

²INOESY S.R.L., 8 Fdc. Mestecanis Street, 707410, Valea Lupului, Iasi, Romania

This paper presents results from a five and half-year study (2015-2020) at an ACTRIS station located in Măgurele, Romania focusing on lidar calibration and assessment of correction factors to improve data accuracy from a multiwavelength Raman polarization lidar operating since 2008. The lidar system was used to measure atmospheric aerosols. Regular quality assurance tests were performed, and all datasets were processed with the Single Calculus Chain software. The analysis revealed that the lower troposphere had more fine particles than the upper troposphere, and the highest Ångström exponent values were reached in autumn and summer. With a careful calibration, lidar technology can be used for determining the aerosol optical and microphysical parameters at the quality necessary for accurate radiation calculations and for the prediction of aerosol–climate effects.

(Received March 2, 2023; accepted April 5, 2023)

Keywords: Aerosols, Troposphere, Multiwavelength Raman lidar, Calibration, Optical and microphysical parameters

1. Introduction

Atmospheric composition is a complex and ever-evolving phenomenon, with far-reaching implications for the climate system. For example, the atmosphere composition is determined by natural and human-related emissions, as well as the energy exchanges between the atmosphere, the Earth's surface and the sun. Gases such as NO, NO₂, HONO, HNO₃, NH₃, SO₂, DMS, Biogenic VOC, O₃, CH₄, N₂O and particles between 1nm and a few micrometers in size are all components of the atmosphere [1]. The physical state of the atmosphere also varies considerably with location, in particular with altitude and latitude. Studying atmospheric composition requires an extensive array of techniques, instrumentation, and methodologies. Research aircraft, laboratory facilities, advanced analytical instrumentation and/or monitoring stations are used to validate numerical models of the atmosphere. This data must be of known quality in terms of precision, accuracy, and representativity [2]. Campaigns are conducted to acquire a better understanding of microphysical systems, while long-term observations spanning multiple temporal scales are needed to validate models and assess trends [3]. Instruments measure particle number and mass concentration, size distribution, water uptake, optical properties, chemical composition, black carbon, and interaction with clouds. Advanced analytical techniques are used to study atmospheric composition, while state-of-the-art atmospheric modelling is used to study atmospheric change processes. Long-term global and regional atmospheric observations are used to quantify

and understand the current perturbation of the atmospheric cycles of reactive species and aerosols. Instrumented passenger aircraft, ground-based in situ and remote sensing stations, and earth observation satellites are used to study atmospheric composition [3].

Atmospheric aerosols are small particles suspended in the air that can have a wide range of properties and lifetimes, depending on their origin, composition, and environment [4]. The size of the aerosols can affect their ability to scatter and absorb light, as well as their ability to interact with other atmospheric constituents, such as clouds and precipitation [5]. They can be made up of a variety of different compounds, including mineral dust, sea salt, sulfuric acid, organic compounds, and black carbon [6]. The composition of the aerosols can affect their properties, such as their optical properties and ability to interact with other atmospheric constituents. Atmospheric aerosols can be generated by a variety of sources, including natural sources, such as volcanic eruptions and wind-blown dust, and human-made sources, such as combustion of fossil fuels and industrial processes.

Optoelectronic techniques are commonly used to detect and characterize atmospheric aerosols. These involve using optical or laser technology to measure the properties of aerosols [7, 8, 9]. The polarization lidars, for example, are becoming key optoelectronic instruments for determining particle shape information [10]. The retrieval of aerosol microphysical properties from multiwavelength lidar data requires the availability of the backscatter coefficient at 3 wavelengths and of the extinction coefficient at 2 wavelengths, allowing for the derivation of

the aerosol size distribution [11] and the particle concentration [12]. Lidar systems can be ground-based or mounted on aircraft or satellites, providing a vertical profile of atmospheric composition from the surface to the upper atmosphere. Depending on the design and the power of the system, a lidar can probe the atmosphere from 0.8 km up to 20 km altitude [13]. The lidar emits short laser pulses into the atmosphere which is then scattered by atmospheric particles and molecules, some of the scattered light being reflected back towards the instrument, collected by a telescope, optically analysed by a wavelength separation unit and then converted into electrical signal by means of sensitive photodetectors [14]. The time delay between the laser pulse and the return signal is used to determine the range to the scattering target, and the intensity of the return signal provides information about the properties of the target.

In high repetition rate laser-based lidar systems, the laser operates at a high pulse repetition rate, typically in the kHz to MHz range, which enables the instrument to make a large number of range measurements per second [15]. This results in high temporal resolution, which is useful for studying fast-evolving atmospheric processes, such as turbulence and convection [16]. Additionally, the high repetition rate allows for a large number of measurements to be taken over a short period of time [17]. Low repetition rate, high power lidar systems typically use lasers with low pulse repetition rates, on the order of several pulses per second, but with high pulse energy, typically several mJ or more [18]. The low repetition rate and high power of these lasers enable the system to probe deeper into the atmosphere, and to measure larger particles, such as cloud droplets and ice crystals [19]. The high pulse energy also allows for improved measurement precision, as the return signal is stronger and less affected by noise [20].

Multi-wavelength polarisation lidars are powerful tools for studying the backscattering of particles in the atmosphere. By using the Stokes vector and Mueller matrices formalism, the lidar particle depolarization ratio can be evaluated [21]. The depolarization ratio is the ratio of the polarized to total backscattered light, and it can provide information about the shape and composition of the aerosol particles. This provides a robust description of the polarisation state of the incident and backscattered radiations and allows for a robust calibration of the lidar device [22]. Furthermore, the scattering matrix for a multi-wavelength lidar can be determined by analyzing the depolarization ratio and color ratio of the backscattered light at different wavelengths. The color ratio is the ratio of the backscattered light at two different wavelengths. This process typically involves inversion algorithms that use a combination of theoretical models and experimental measurements to estimate the scattering properties of aerosol from the lidar data [23].

2. Instruments and methodology

2.1. Instruments and data quality assurance

In this study, the active remote sensing systems from the aerosol remote sensing laboratory, part of the ACTRIS observational platform operated by the National Institute of Research and Development for Optoelectronics INOE 2000, located in Măgurele, Romania were used. ACTRIS is a European research infrastructure dedicated to the study of atmospheric aerosols, clouds, and trace gases [24]. The main goal of ACTRIS is to provide researchers with access to high-quality, long-term observational data on atmospheric aerosols, clouds, and trace gases, as well as to support the development of new techniques and methods for characterizing atmospheric composition and climate. The infrastructure is made up of a network of ground-based stations and an aircraft platform, which are equipped with state-of-the-art instruments and sensors for measuring various atmospheric properties. ACTRIS was established in 2009 and is currently supported by over 40 institutions across Europe (www.actris.eu).

According to ACTRIS standards, the optimal configuration of an aerosol remote sensing station consists of a Raman or high spectral resolution lidar operating at 3 wavelengths with the ability to determine polarization, and a sun/sky/lunar photometer. The multiwavelength Raman polarization lidar (RALI) operating since 2008 in Măgurele, Romania is an atmospheric lidar system that uses low repetition, high-power laser and the Raman scattering technique to measure the properties of atmospheric aerosols and trace gases. The system is equipped with multiple wavelengths that allow it to detect a wide range of atmospheric species, including water vapor and nitrogen. The RALI system uses polarization measurements to retrieve information about the size, shape, and composition of aerosol particles in the atmosphere. The multi-wavelength aspect of the lidar allows it to probe the atmosphere at different wavelengths, which can provide information about the particles' microphysical properties and types. The high-power aspect of the lidar increases the distance it can probe into the atmosphere, providing a more comprehensive view of the particle distribution. The polarization capability of the lidar allows it to measure the polarization properties of the scattered light, providing information about the shape and orientation of the particles.

When analysing the data products, however, one has to be aware that any aerosol high-power lidar system has several optical and electronic limitations and problems that can affect their performance and accuracy [25]: a) signal attenuation due to scattering and absorption by aerosols and other atmospheric components, which limits the lidar's range and sensitivity; b) background noise from solar radiation, skyglow, and other sources, which can interfere with the lidar signal and reduce its signal-to-noise ratio; c) crosstalk and interference between different lidar channels and components, which can cause errors and reduce the lidar's accuracy and precision; d) laser damage and degradation from prolonged high-power operation, which

can reduce the lidar's output power and shorten its lifespan; e) electronic noise and drift in the lidar's detectors and amplifiers, which can reduce the signal quality and introduce errors; f) difficulty in calibrating and validating the lidar's measurements, due to the complex and variable nature of the atmospheric aerosol distribution [26].

In order to better assess the performances of the aerosol lidars and allow uncertainty estimates, the European Aerosol Research Lidar Network (EARLINET) which is now part of ACTRIS has developed quality assurance tests for aerosol lidars to ensure the accuracy and reliability of aerosol measurements [27]: calibration, range, signal-to-noise, pulse width, background noise, accuracy and data quality tests. Calibration tests involve verifying the accuracy of the instrument's optical and electronic components and ensuring that the instrument is properly calibrated. Range tests involve verifying the accuracy of the instrument's range measurements and ensuring that the instrument is capable of accurately measuring aerosols over the desired range. Signal-to-noise ratio tests involve verifying the accuracy of the instrument's signal-to-noise ratio and ensuring that the instrument is capable of accurately measuring aerosols even in noisy conditions. Pulse width tests involve verifying the accuracy of the instrument's pulse width measurements and ensuring that the instrument is capable of accurately measuring aerosols over a wide range of pulse widths. Background noise tests involve verifying the accuracy of the instrument's background noise measurements and ensuring that the instrument is capable of accurately measuring aerosols even in noisy conditions. Accuracy tests involve verifying the accuracy of the instrument's measurements and ensuring that the instrument is capable of accurately measuring aerosols over a wide range of conditions [28]. Data quality tests involve verifying the quality of the instrument's data and ensuring that the data is accurate, reliable, and suitable for further analysis.

Depolarization calibration is another critical step in the process of using aerosol high-power lidars to measure atmospheric aerosols. In this process, the lidar system is calibrated to accurately measure the degree of polarization of the light scattered by aerosols [29]. The degree of polarization is a measure of the degree to which the light is linearly polarized, and can provide important information about the size, shape, and composition of the aerosols being measured [30]. To evaluate depolarization due to air particles and molecules, factors such as an incomplete polarization of the laser source, non-ideal behavior of the polarizing beam splitter, and differing gain factors between the parallel and perpendicular channels must be considered. As a result, calibration of a polarization lidar is critical for providing correct atmospheric observations. Observations in aerosol and cloud free regions are typically used to determine the instrument gain ratio of the two polarization channels, with the assumption that the observed ratio in these cases is equal to the molecular depolarization ratio obtained through theoretical calculations [31] or observational data [32]. The

disadvantage of this approach is that little amounts of undetected aerosols can generate considerable inaccuracies. Furthermore, molecular depolarization must be precisely characterized. Given that the lidar detected molecular depolarization ratio can range from 0.36% to 1.4% depending on lidar receiver spectral width and may be temperature dependent [33], inaccuracies owing to presumed molecular depolarization ratio can be considerable. Another way of calibrating employs unpolarized light to provide identical signals on both channels [34]. However, unpolarized light is difficult to produce, especially in the field. A single detector technology, switching optics to detect the two polarizations for alternate laser pulses, can also be employed [35]. In this procedure, however, the optical reflectance and transmission properties of a polarizing beam splitter (PBS) must be known. These parameters are difficult to estimate and can alter dramatically due to not just polarizing cube misalignment but also non-ideal light beam collimation, particularly for broad spectral band prisms [36]. Another calibration method is to generate a balanced signal on both detectors by insertion of a half-wave plate into the optical path of either the transmitter or receiver [37].

EARLINET-ACTRIS has proposed and implemented the 90 deg polarisation calibration, which is usually performed by rotating the polarizing element in the lidar system to a 90 degree orientation and measuring the change in the depolarization ratio [38]. The change in the depolarization ratio is used to determine the accuracy of the polarimeter and to make any necessary adjustments to ensure accurate measurements [14]. The 90 degree calibration is important because the accuracy of the depolarization ratio measurements is sensitive to the orientation of the polarizing element. Any misalignment of the polarizing element can result in incorrect measurements and lead to errors in the retrieval of aerosol properties and the assessment of the atmospheric state [39]. The 90 degree calibration should be performed regularly to ensure the accuracy of the polarimeter and to correct for any changes in the orientation of the polarizing element that may occur during operation. The frequency of the 90 degree calibration depends on the stability of the polarimeter and the operational environment, but it is typically performed several times per year.

RALI detects backscattered signal from aerosols and molecules in elastic (1064 total, 532 parallel, 532 cross, 355 total) and Raman (607 total, 387 total) channels, as well as water vapor (408 total). Atmospheric structure (time series of aerosol and cloud layers) is measured with a vertical resolution of 3.75 m and a temporal resolution of 1 min. The instrument operates according to the predefined schedule and during intensive measurement periods [13] and complies with the EARLINET-ACTRIS quality assurance protocols.

EARLINET-ACTRIS quality assurance tests are performed periodically (weather permitting) in order to check the status of the instrument, identify possible misalignments or damages on the optics and electronics.

2.2. Lidar data processing and analysis

Aerosol optical parameters (backscatter coefficients at 1064, 532 and 355 nm, extinction coefficients at 532 and 355 nm and linear depolarization ratio at 532 nm) are calculated using the ACTRIS centralized processing chain (Single Calculus Chain, SCC), usually as 1-hour profiles from 0.5 to 15 km altitude [40, 41]. The EARLINET-ACTRIS Single Calculus Chain [42] is a standard data processing and calibration platform used to retrieve aerosol optical properties from lidar measurements, such as the aerosol backscatter coefficient and the depolarization ratio. The accuracy of the retrieval of the aerosol optical properties depends on the accuracy of the correction and calibration procedures, as well as the quality of the raw lidar signals. The chain starts with the raw lidar signals and applies various correction and calibration procedures to obtain the final aerosol optical properties. The calculation of the aerosol optical properties involves several steps, implemented as software modules.

The HiRELPP (High Resolution Lidar Processing Package) module is used to correct and calibrate high-resolution lidar signals [41]. The aim of the pre-processing is to correct for various sources of instrumental and atmospheric artifacts in the raw lidar signals and to prepare the data for the retrieval of aerosol optical properties. Background correction accounts for the residual background signal in the raw lidar signals, which can be caused by atmospheric molecular backscatter and scattered light from the instrument itself. Range correction accounts for the range-dependent intensity decrease in the raw lidar signals due to the attenuation of the laser beam by the atmosphere. Wavelength calibration corrects for any wavelength-dependent intensity variations in the raw lidar signals. This is performed using an auxiliary channel, such as a Sun photometer, which measures the spectral dependence of the atmospheric transmission. Molecular backscatter correction removes the contribution of the atmospheric molecular backscatter to the raw lidar signals. This is performed using a model that predicts the molecular backscatter based on atmospheric temperature and pressure profiles.

The ELDA (Earlinet Lidar Data Analysis) module is used to retrieve aerosol optical properties, such as extinction, backscatter and depolarization, and to derive the vertical distribution of atmospheric aerosols from the corrected and calibrated lidar signals [40]. The aerosol backscatter coefficient is used to retrieve the aerosol optical depth and to assess the atmospheric aerosol load. The depolarization ratio provides information about the orientation of the atmospheric particles with respect to the laser beam and can be used to retrieve particle size and shape. The ELDA module also includes quality control procedures to ensure that the data obtained is reliable and consistent.

The calibration – processing chain presented above was used further to compile a statistical analysis of the aerosol intensive optical parameters based on five years of lidar data (Jan. 2015 – May 2020). The backscatter coefficient profile at the highest available wavelength (in

this case 1064 nm), determined with SCC, was used to determine the aerosol layer boundaries according to the methodology described in Belegante et al. (2014) [43]. For each identified layer, the mean values of backscattering coefficients, extinction coefficients and particle depolarization ratio were calculated, from which we calculated intensive optical parameters (Ångström exponent and lidar ratios) as follows:

Ångström exponent

$$AE = \frac{\ln\left(\frac{\alpha_{355}}{\alpha_{532}}\right)}{\ln\left(\frac{355}{532}\right)} \quad (1)$$

Lidar ratio at 532 nm:

$$LR = \frac{\alpha_{532}}{\beta_{532}} \quad (2)$$

Lidar ratio at 355 nm:

$$LR = \frac{\alpha_{355}}{\beta_{355}} \quad (3)$$

where α_{355} and α_{532} represent the extinction coefficients and β_{355} and β_{532} represent the backscatter coefficients at 355 and 532 nm wavelengths [43].

The obtained values were filtered to exclude physically impossible cases (due in general to incomplete filtering of clouds from the measured data), more specifically, layers where the Ångström exponent is greater than 3 or less than -3 were excluded from the statistical analysis, such as and those where the lidar ratios are greater than 200 sr or less than 10 sr. Thus, 453 data sets corresponding to as many aerosol layers were obtained. Of these, the lowest identified layer was considered representative of the lower troposphere, the other layers being considered representative of the upper troposphere.

3. Results and discussion

3.1. Lidar hardware calibration

Fig. 1 presents the telecover test results for 355 and 532 nm channels retrieved using the RALI system. The telecover test is used to assess the laser/telescope alignment for the near range altitudes and to highlight potential issues in the receiving unit of the instrument [27]. The normalised RCS (range corrected signal) and RAW signals at 355 nm show a good agreement with the results indicated by Freudenthaler et al. (2018) [27]. The two North signals indicate a good atmospheric stability with some aerosol layers below 1000 m. The North signals are collected to assess the atmospheric stability during the entire test (one at the beginning of the test and the second at the end of the telecover test).

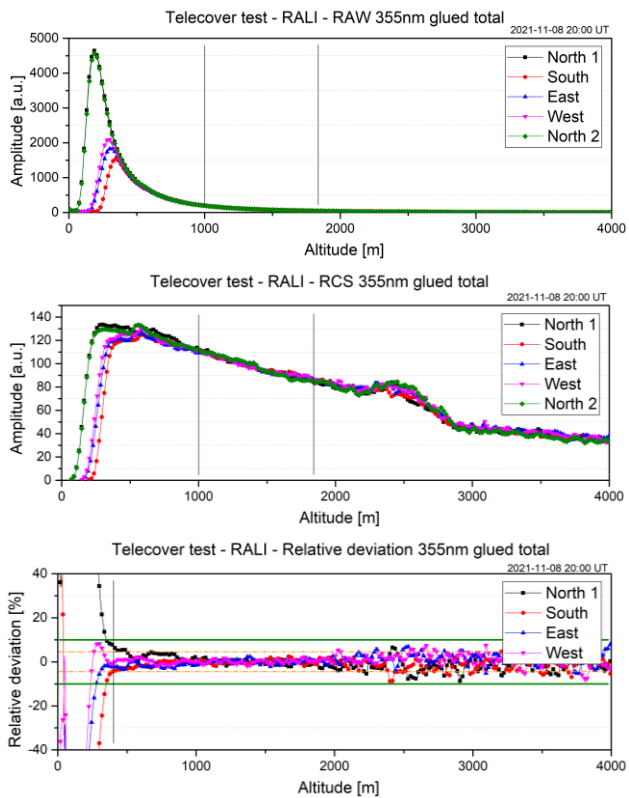


Fig. 1. Telecover test results for the 355 nm channel. Normalized RAW and RCS signals; Relative deviation from the mean signal (color online)

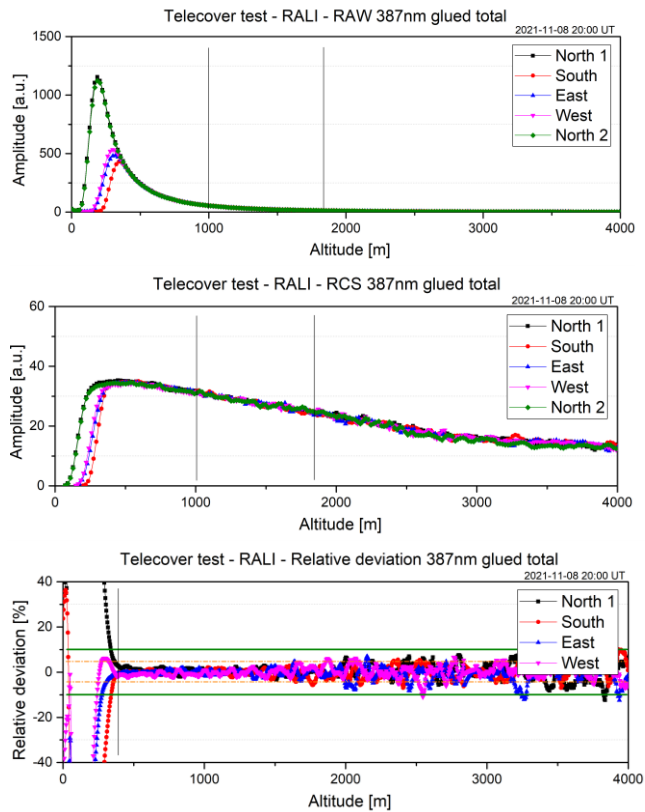


Fig. 2. Telecover test results for the 387 nm channel. Normalized RAW and RCS signals; Relative deviation from the mean signal (color online)

The signal on East and West sectors shows similar amplitudes for the RAW signals, indicating a good alignment on the E-W axes. The relative deviation plot indicates that all signals fall under the 10% criterion below 500 m [27]. This criterion indicates a complete overlap around 500 m. The normalised RCS and RAW signals at 387 nm channel show similar results for the 355 nm wavelength Fig. 2. For this case, the atmospheric layers found below 1000 m have fewer effects on the signal amplitude. The relative deviation plot indicates that all signals fall under the 10% criteria around 450 m. Since the effects of the atmospheric layers are not significant, a more accurate overlap estimate can be retrieved. The telecover test indicates a full overlap above 450 m. Based on the optical specifications of the instrument (Field of View 1.7 mrad, laser divergence of 0.3 mrad (86.5% criteria), telescope mirror diameter of 400 mm and a theoretical overlap of 800 m for perfectly oriented emission - receiver axes), the 387 nm overlap indicates a laser tilt of 0.3 mrad (corresponding to a near range optimization of the instrument).

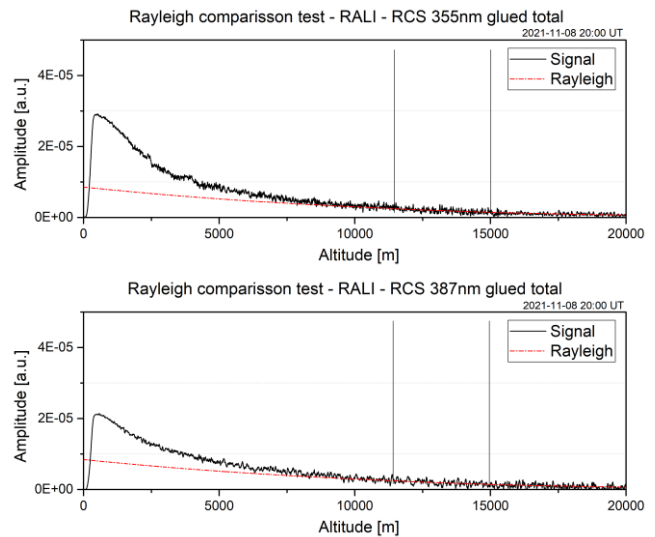


Fig. 3. Rayleigh fit test results for 355 and 387 nm channels. Normalized RCS signals: 11000-15000 m normalization range (color online)

The Rayleigh Fit test is used to assess the far range alignment of the lidar instrument. Results for the 355 and 387 nm channels indicate a good alignment in this range (Freudenthaler 2018) [27].

Fig. 3 shows that the normalised lidar signals do not drop below the Rayleigh molecular signal.

3.2. Retrieval of the aerosol optical parameters

Fig. 4 shows an example of RALI data products obtained with the Single Calculus Chain for 8 March 2021. The time series are obtained with the HiRELPP module, and the aerosol optical parameters are obtained with the ELDA module of the SCC.

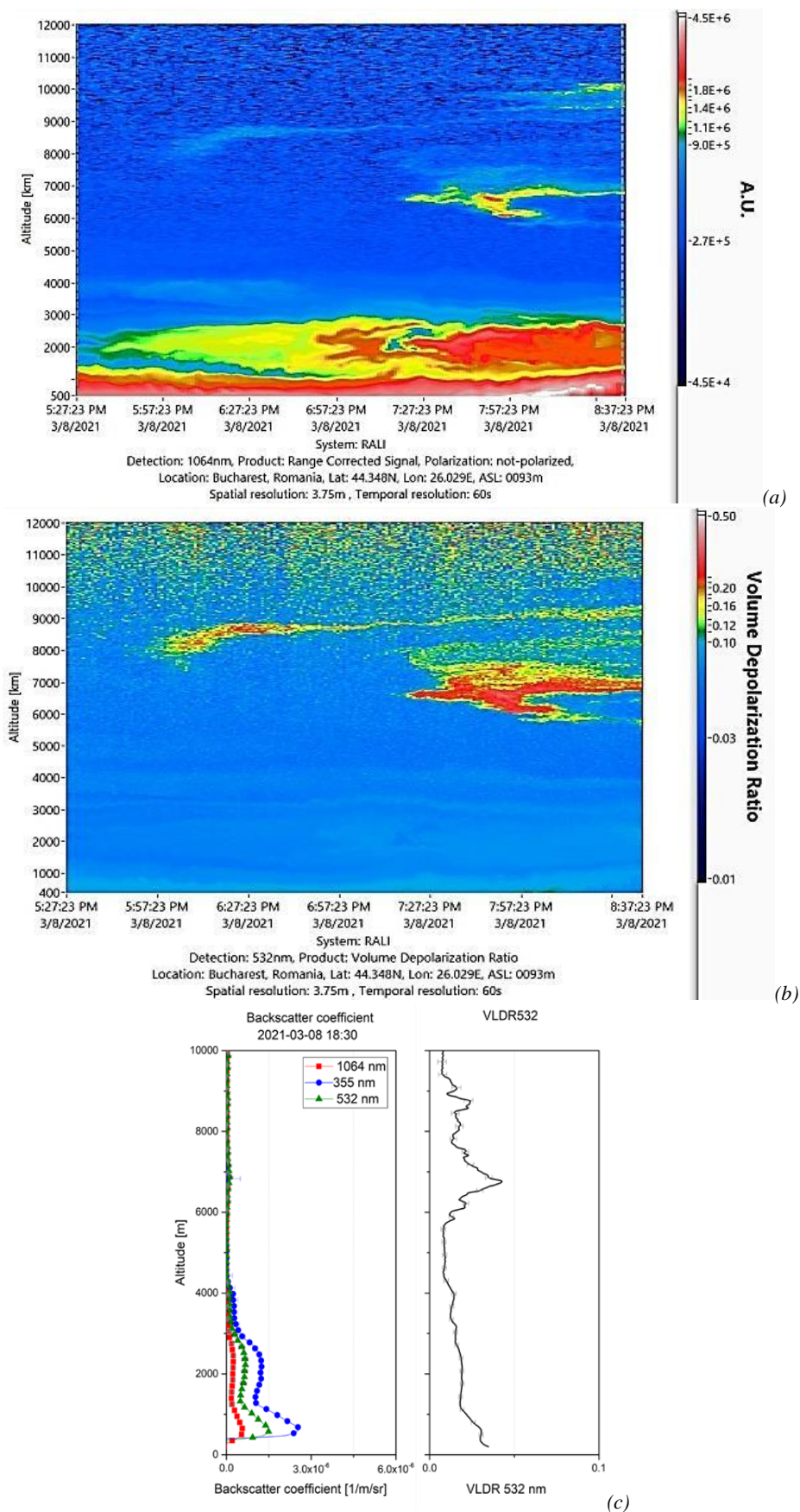


Fig. 4. Time series of range-corrected signal (upper left panel), volume depolarization (lower left panel), and aerosol optical parameter profiles (backscatter coefficient at 1064, 532, and 355 nm and volume depolarization ratio at 532 nm, respectively, right panel) measured with the lidar system at Magurele on March 8, 2021 (color online)

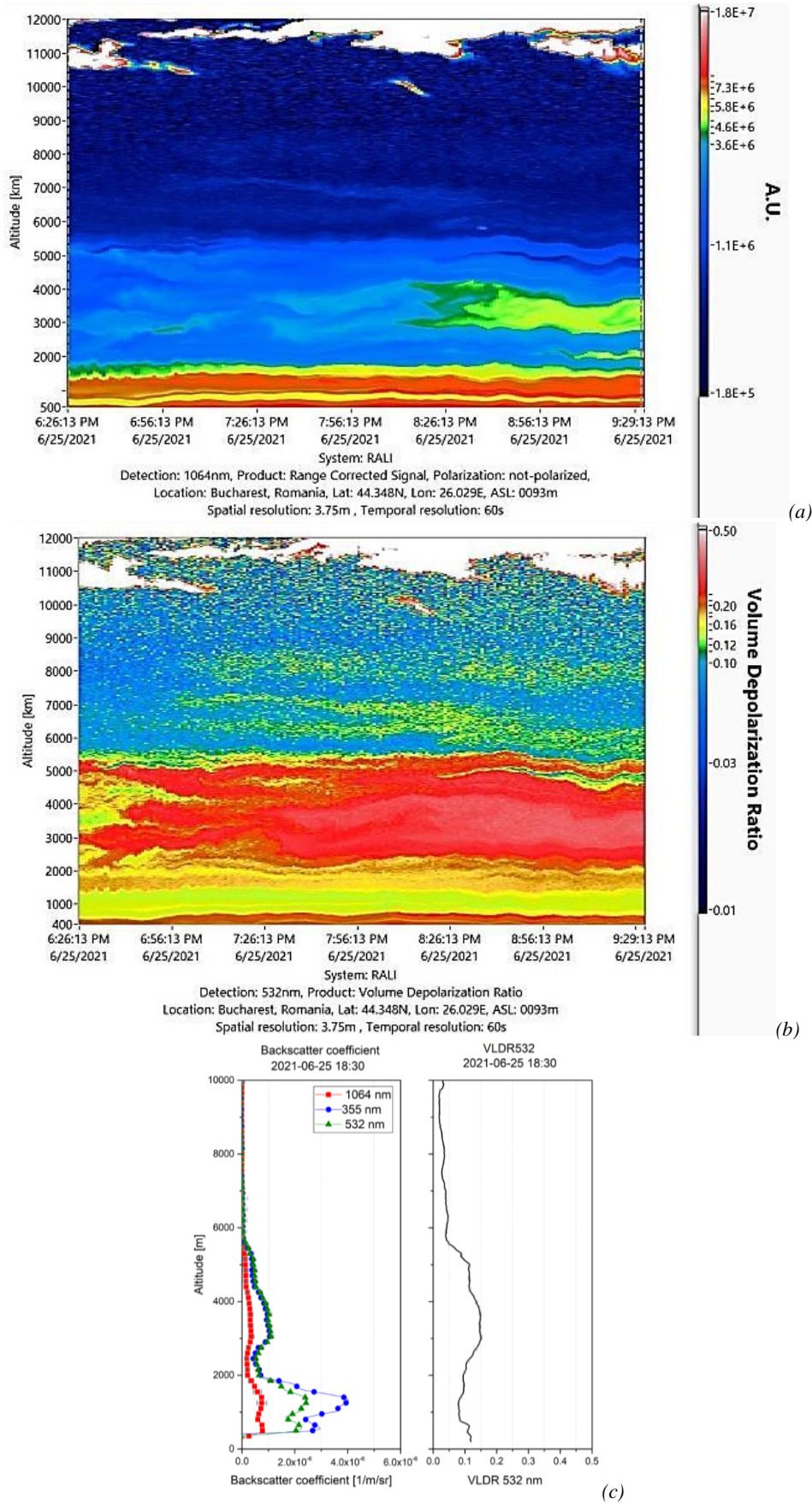


Fig. 5. Time series of range-corrected signal (a), volume depolarization (b), and aerosol optical parameter profiles (backscatter coefficient at 1064, 532, and 355 nm and volume depolarization ratio at 532 nm), (c) measured with the lidar system at Măgurele on June 25, 2021 (color online)

Profiles are obtained as averages of profiles measured over one hour. Averaging is done to obtain a sufficient signal-to-noise ratio for the application of the inversion algorithms, the profiles measured with a temporal resolution of 1 minute being too noisy to calibrate the signal in the molecular region (above 20 km altitude).

This is also the reason why optical parameter profiles cannot be calculated if low clouds are present that the laser radiation cannot penetrate. The processing algorithms first identify the presence of clouds and exclude them from the time series. If the remaining profiles are not sufficient to calibrate in the molecular region, then the optical parameters are not calculated. Analysis of the products obtained for March 8, 2021 shows that the planetary boundary layer was up to 1.2 km high and that several layers of aerosols are present.

Thus, the layer that can be seen at 3.0 km shows a small volume depolarization, typical of spherical particles, and also has a spectral behaviour indicating a large Ångström exponent, hence small particles. Also, a fine layer is present at the altitude of 7.0 km, with a larger volume depolarization, indicating aerosols in the process of activation. The low backscatter coefficient values for that layer correspond to a low aerosol loading compared to the planetary boundary layer and the 3.0 km layer.

In Fig. 5 the lidar observation of June 25, 2021 is presented, pin pointing an example of range corrected signals time series, profiles of backscatter coefficients at three wavelengths, as well as the volume linear depolarization ratio. The presence of cirrus clouds at an altitude of 10.0 –12.0 km is not likely to prevent calibration because, on the one hand, they are high enough to find a calibration altitude, on the other hand, cirrus clouds are penetrated by laser radiation, so the lidar signal is still useful beyond 12.0 km. From the time series of the range-corrected signal and volume depolarization a sub-structure within the planetary boundary layer can be observed, successive layers of aerosols exhibiting increased depolarization is typical for mineral dust intrusions, but the confirmation of this fact cannot be obtained only from the analysis of the extensive optical parameter profiles, as it is necessary to effectively identify the altitude of the layers and calculate the intensive optical

parameters inside the layer. Based on these, coupled with other data sources such as solar photometry or air mass trajectory analysis (which estimates the likely source), the likely type of aerosol can be identified. Aerosol type can also be estimated from lidar data if the set is complete (i.e. extinction profiles are also available) using advanced classification methods [44]. Finally, the type of aerosol can be identified if the microphysics parameters (dimensional distribution, complex refractive index) can be calculated.

At altitudes above 10.0 km, cirrus clouds are present. A consistent layer of non-spherical particles extending from 1.5 to 5.5 km is also observed. For this layer, the volume depolarization is high, over 15%, which indicates the presence of some non-spherical particles in the layer. The values of the backscatter coefficients at 532 nm and 355 nm are very close inside the layer, a typical spectral behaviour for large-sized particles.

A completely different example is shown in Fig. 6 for March 19, 2022.

Time series of range-corrected signal and volume depolarization show that the planetary boundary layer reaches 2.0 km altitude and that there are downward motions within it that allow particle transport to the earth's surface. Of interest, however, is the descending layer of spherical particles from 3.5 – 5.0 km which, although clearly visible in the distance-corrected signal, is not at all visible in the volume depolarization.

Moreover, its values in the layer are only 1.5% (compared to values of 15% in the case presented for the day of June 25, 2021 or values of 4% typical for the mixing layer in the example of the day of March 8, 2021). This fact indicates the preponderance of spherical particles in the layer. The typical spectral behavior for small particles is also observed, the values of the backscattering coefficients at the 3 wavelengths being very different. Above this layer formed, most probably, of smoke particles, a second very fine layer can be observed, at 8.0 km altitude. According to the volume depolarization values (significantly higher than those in the lower layer) this layer appears to contain a small proportion of non-spherical particles.

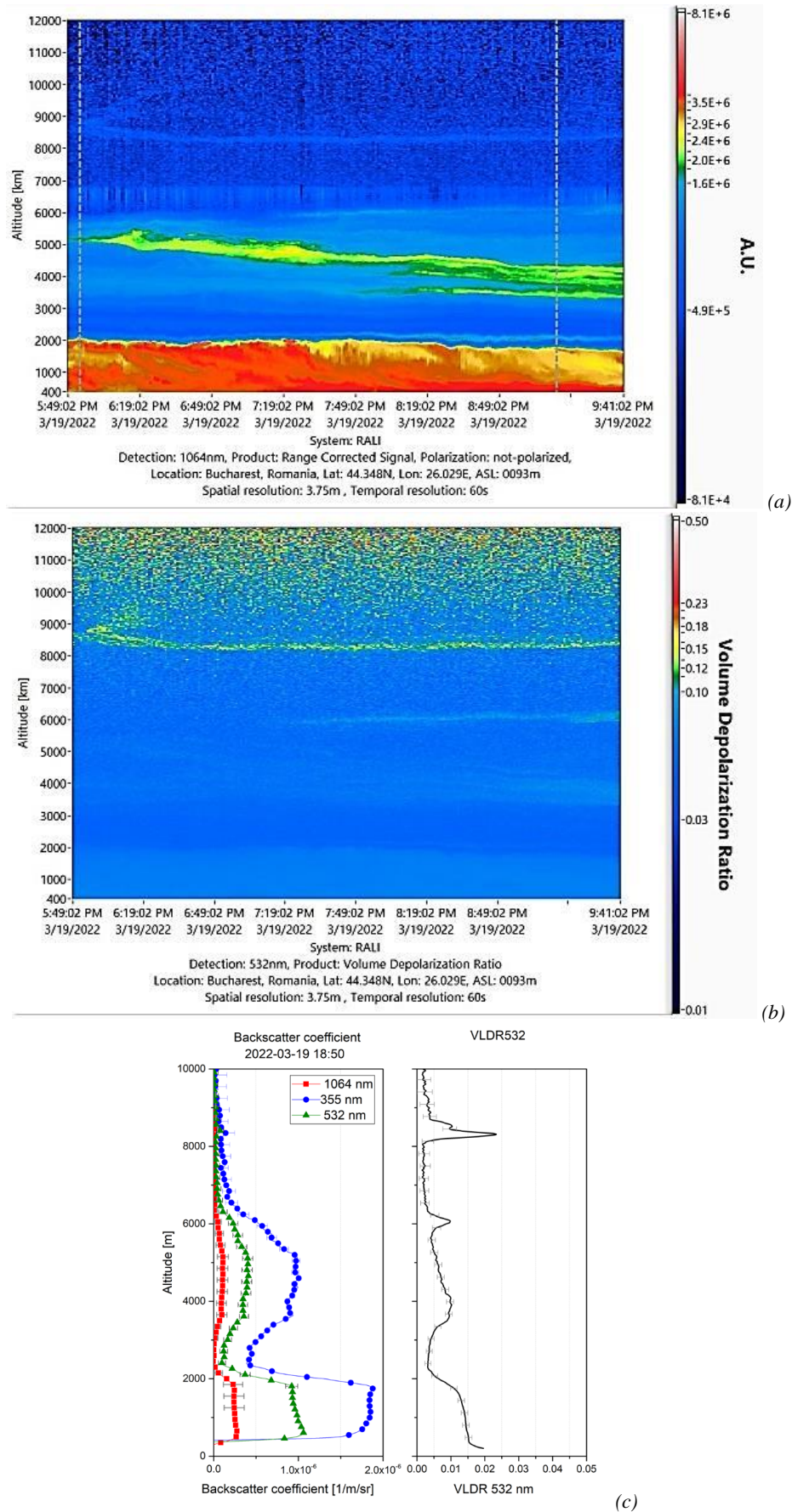


Fig. 6. Time series of range-corrected signal (a), volume depolarization (b), and aerosol optical parameter profiles (backscatter coefficient at 1064, 532, and 355 nm and volume depolarization ratio at 532 nm), (c) measured with the lidar system at Măgurele on March 19, 2022 (color online)

3.3. Aerosol properties using the calibrated multi-wavelength polarisation lidar

Fig. 7 presents the result of the statistical analysis for the entire period January 2015 – May 2020, comparison between the intensive optical parameters of the aerosol

from the low troposphere (in black) and the high troposphere (in blue).

It can be seen that the average value of the Ångström exponent in the lower troposphere is higher than in the upper troposphere, indicating smaller particle size.

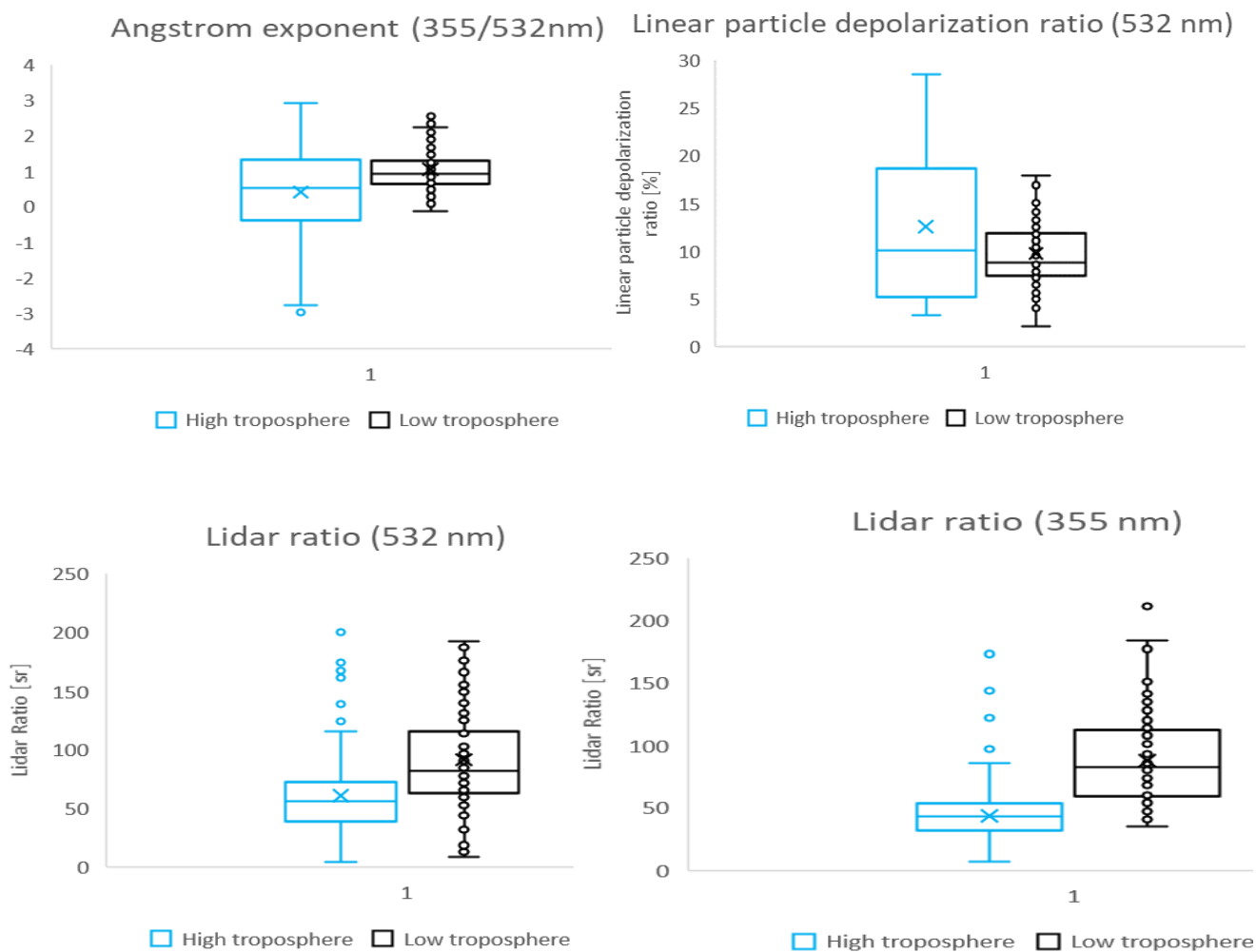


Fig. 7. Averages of intensive optical parameters in the aerosol layers of the low (black) troposphere and high (blue) troposphere at Măgurele for the period January 2015 – May 2020: Ångström exponent (top left panel), linear particle depolarization ratio (top right panel) and lidar ratios at 532 and 355 nm respectively bottom panels) (color online)

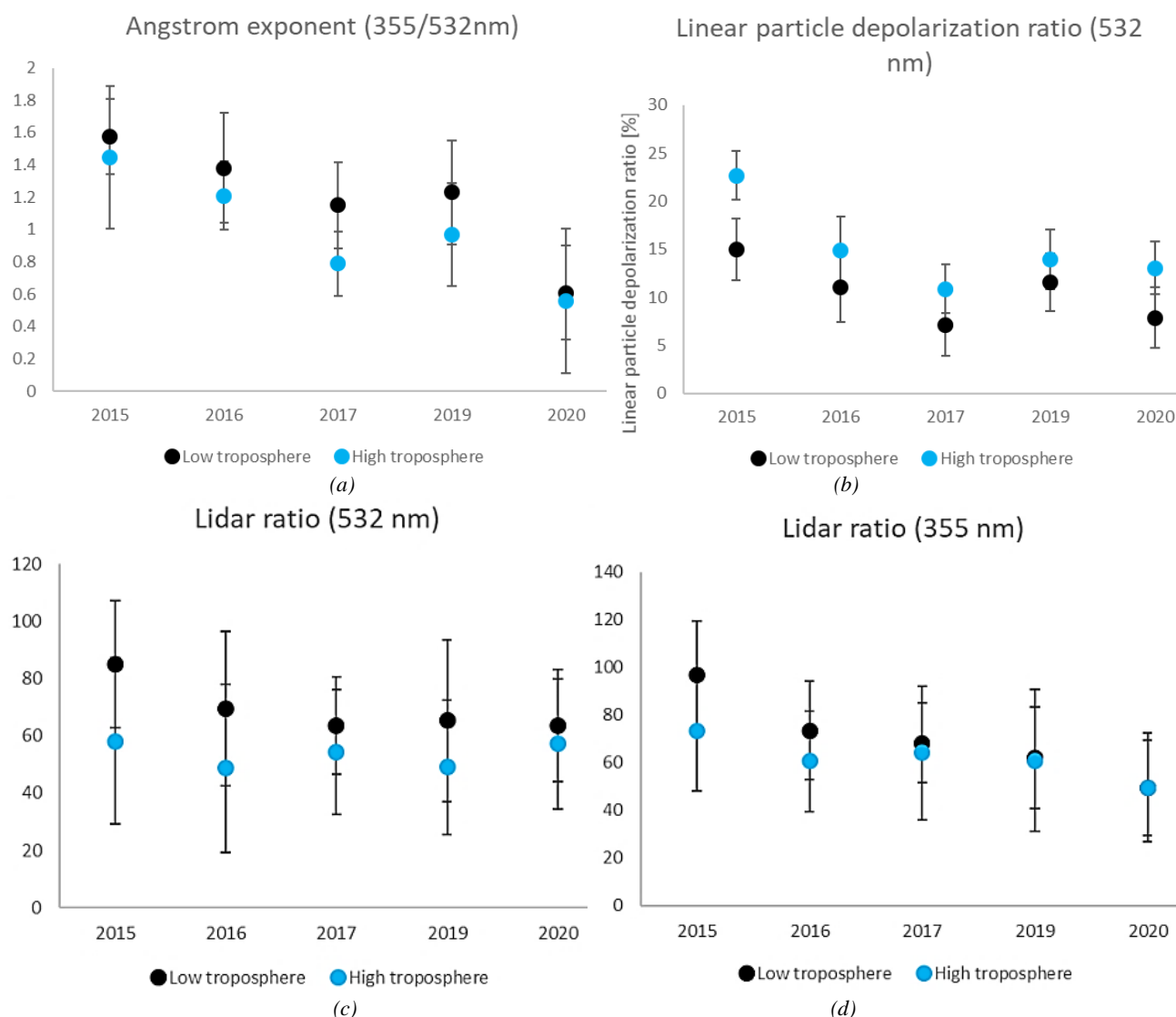


Fig. 8. Annual variations of intensive optical parameters in the aerosol layers of the low (black) and high (blue) troposphere at Magurele for the period January 2015 – May 2020: Ångström exponent (a), linear particle depolarization ratio (b) and lidar ratios at 532 and 355 nm (c, d) (color online)

The scatter in the data is greater in the upper troposphere, indicating greater variability in particle sizes than in the lower troposphere. The linear depolarization ratio of the particle is higher in the upper troposphere, probably due to the transport periods of the mineral dust, which is nonspherical in shape. Lidar ratios at both wavelengths are higher in the lower troposphere where the most significant proportion of absorbing particles from traffic or industry is concentrated.

Fig. 8 shows the annual averages of intensive optical parameters in the aerosol layers measured between January 2015 and May 2020, comparing the low troposphere (in black) and the high troposphere (in blue).

The Ångström exponent shows similar values in the 2 regions of the atmosphere, slightly lower in the high troposphere but within the uncertainty limit. The years 2015 and 2016 were marked by significant production and transport of aerosols from biomass burning [45], which led

to higher values of the Ångström exponent, with a slight decrease afterwards.

A slight decrease of linear particle depolarization and lidar ratios values can be observed, with higher values of linear particle depolarization ratio in the high troposphere due to the presence of bigger and non-spherical particles. Next, we analyzed the seasonal variations of the intensive optical parameters of the aerosol in the chosen period (Fig. 9). Thus, the values corresponding to the months of March, April and May were averaged and considered representative for the spring season, those corresponding to the months of June, July and August for the summer season, etc. The results obtained are presented as a comparison between the low troposphere (in black) and the high troposphere (in blue).

It can be seen that the values of the Ångström exponent are consistently higher in the lower troposphere regardless of the season, indicating that the upper troposphere is always richer in large-sized particles due to

long-range transport. At the same time, the preponderance of small particles in the lower layers is due to the injection of particles from traffic and industry. The highest values of the Ångström exponent are reached in the autumn in the lower troposphere (probably due to the burning of agricultural waste and the start of residential heating) and respectively in the summer in the upper troposphere (probably due to the intensification of the transport of smoke particles from large fires in regions such as Ukraine and Greece).

The particle depolarization ratio is almost constant in the lower troposphere, regardless of season, indicating a mixture of spherical (predominant) and non-spherical (minor) particles. In the upper troposphere, however, non-

spherical particles are predominant in spring, corresponding to mineral transport from the Sahara Desert. The transport of mineral dust remains at a lower level in summer and autumn but is significantly reduced in winter. This is also visible in the values of the particle depolarization ratio, which decreases in summer and autumn compared to spring, but whose decrease is most pronounced in winter. The lidar reports at both wavelengths behave similarly. Thus, maximum values are measured in winter, higher in the lower troposphere than in the upper troposphere, indicating strongly absorbing particles in both regions of the atmosphere. Lower values occur in summer and autumn. During autumn the differences between the two regions are minimal.

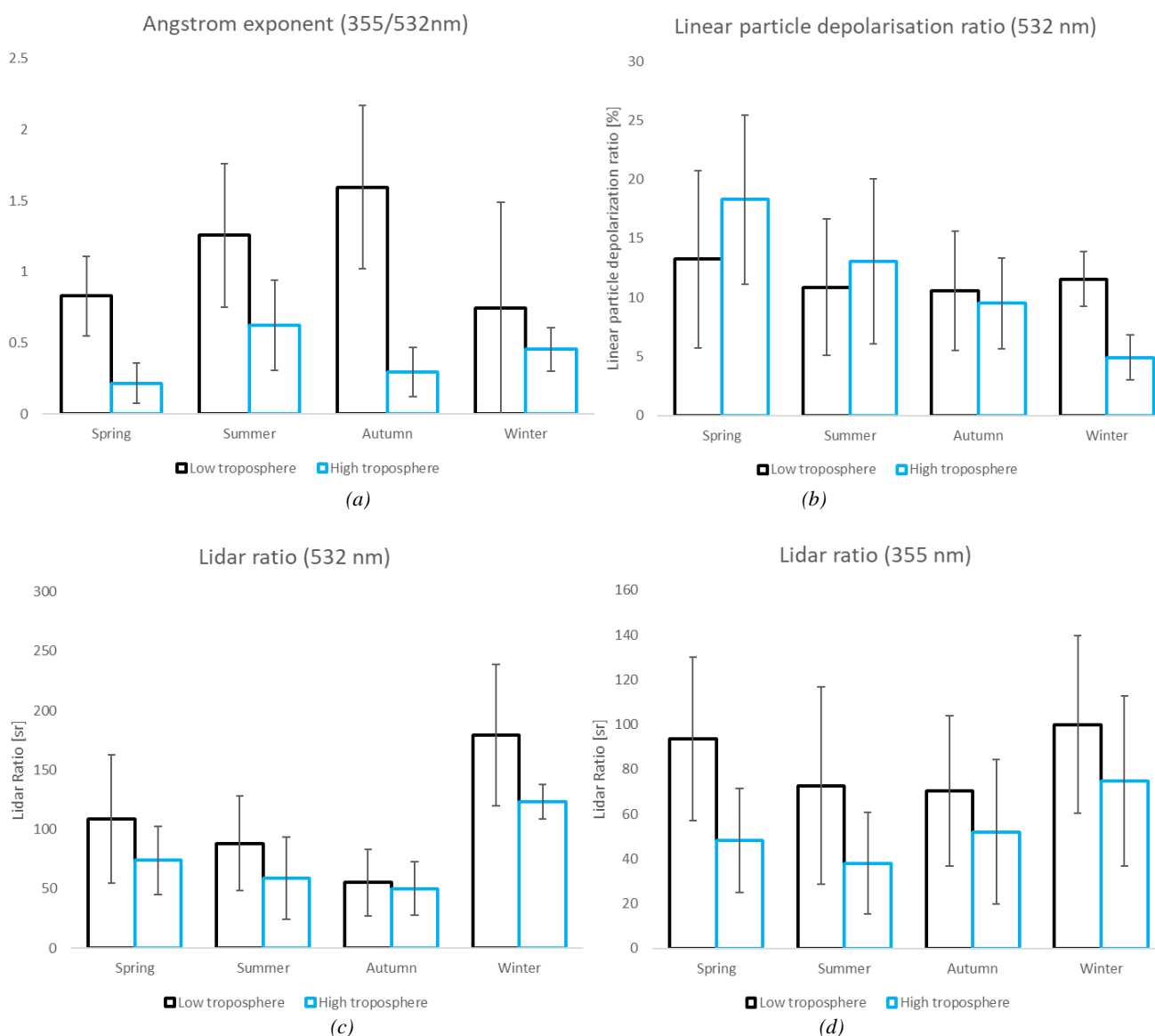


Fig. 9. Seasonal variations of intensive optical parameters in the aerosol layers of the low and high troposphere at Magurele for the period January 2015 – May 2020: Ångström exponent (a), linear particle depolarization ratio (b) and lidar ratios at 532 and 355 nm (c, d) (color online)

4. Conclusions

This paper presents results obtained at the RADO-Bucharest ACTRIS station located in Magurele for a period of five and a half years (January 2015 – May 2020). Special attention was paid to the instrument calibration, testing and assessment of the correction factors, in order to reduce, as possible, the uncertainty of the data products. EARLINET-ACTRIS quality assurance tests were performed periodically (weather permitting) in order to check the status of the instrument, identify possible misalignments or damages on the optics and electronics.

We have illustrated the information that can be extracted from the time series produced by HiRELPP and respectively from the profiles of the extensive optical parameters of the aerosol produced by ELDA, modules of the Single Calculus Chain (SCC) for several representative cases: 8 March 2021, 25 June 2021 and 19 March 2022, corresponding to various atmospheric conditions. The statistical analysis for the entire period 2015-2020 was performed on 453 data sets corresponding to as many aerosol layers with significant aerosol loading. The layer intensive optical parameters calculated from the multiwavelength profiles were averaged for the lower troposphere and separately for the upper troposphere. The comparison between the optical properties of the aerosols in the two vertical regions is made both for the entire period and for each season and year of the mentioned period. We found that the average value of the Ångström exponent in the lower troposphere is larger than in the upper troposphere, indicating smaller particle size in the near-ground layers. Lidar ratios at both wavelengths are higher in the lower troposphere where the most significant proportion of absorbing particles from traffic or industry is also concentrated. From the point of view of annual variability, the years 2015 and 2016 presented higher values of the Ångström exponent, corresponding to a significant transport of aerosols originating from biomass burning. The highest values of the Ångström exponent are reached in autumn in the lower troposphere and summer in the upper troposphere, respectively. The particle depolarization ratio is almost constant in the lower troposphere, regardless of season, indicating a mixture of spherical (predominant) and non-spherical (minor) particles. In the high troposphere, non-spherical particles are predominant in spring, corresponding to mineral transport from desert regions (Sahara, Arabia). In terms of annual variability of the optical parameters, recent years (2017-2020) are characterised by lower values of the linear particle depolarisation ratio both in the low and the high troposphere (with a slight increase in 2019), indicating more spherical particles. The same slight decrease of the lidar ratio at 532 and 355 nm is observed, as well as of the Ångström exponent, indicating that particles are larger than in previous years and less absorbing. Especially in 2020 large particles dominate, this situation being probably related to the reduction of the industrial activity during the pandemic period. However, these conclusions have to be treated with scepticism, considering the significant uncertainty of the data.

Acknowledgements

This work was carried out through the Core Program within the National Research Development and Innovation Plan 2022-2027, with the support of MCID, project no. PN 23 05/ 3.01.2023. Part of the work performed for this study was funded by the Romanian Ministry of Research, Innovation and Digitization, through Program 1-Development of the national research-development system, Subprogram 1.2 - Institutional performance - Projects to finance the excellent RDI, Contract no. 18PFE/30.12.2021. Further support was provided by the European Regional Development Fund through the Competitiveness Operational Programme 2014-2020, Action 1.1.3 Creating synergies with H2020

Programme, project Strengthen the participation of the ACTRIS-RO consortium in the pan-European research infrastructure ACTRIS, ACTRIS-ROC, MYSMIS code 107596 (ctr. no.337/2021).

The research was partially funded by the European Regional Development Fund through the Competitiveness Operational Programme 2014-2020, POC-A.1-A.1.1.1- F-2015, project Research Centre for Environment and Earth Observation CEO-Terra, SMIS code 108109, contract No. 152/2016.

This work was supported by a grant of the Ministry of Research, Innovation and Digitization, CNCS-UEFISCDI, project number PN-III-P1.1-TE-0714, within PNCDI.

References

- [1] D. Fowler, K. Pilegaard, M.A. Sutton, P. Ambus, M. Raivonen, J. Duyzer, D. Simpson, H. Fagerli, S. Fuzzi, J. K. Schjoerring, C. Granier, A. Neftel, I. S. A. Isaksen, P. Laj, M. Maione, P. S. Monks, J. Burkhardt, U. Daemmgen, J. Neirynek, E. Personne, R. Wichink-Kruit, K. Butterbach-Bahl, C. Flechard, J. P. Tuovinen, M. Coyle, G. Gerosa, B. Loubet, N. Altimir, L. Gruenhage, C. Ammann, S. Cieslik, E. Paoletti, T. N. Mikkelsen, H. Ro-Poulsen, P. Cellier, J. N. Cape, L. Horváth, F. Loreto, Ü. Niinemets, P. I. Palmer, J. Rinne, P. Misztal, E. Nemitz, D. Nilsson, S. Pryor, M. W. Gallagher, T. Vesala, U. Skiba, N. Brüggemann, S. Zechmeister-Boltenstern, J. Williams, C. O'Dowd, M. C. Facchini, G. de Leeuw, A. Flossman, N. Chaumerliac, J. W. Erisman, *Atmos. Environ.* **43**(33), 5193 (2009).
- [2] P. S. Monks, C. Granier, S. Fuzzi, A. Stohl, M. L. Williams, H. Akimoto, M. Amann, A. Baklanov, U. Baltensperger, I. Bey, N. Blake, R. S. Blake, K. Carslaw, O. R. Cooper, F. Dentener, D. Fowler, E. Fragkou, G. J. Frost, S. Generoso, P. Ginoux, V. Grewe, A. Guenther, H. C. Hansson, S. Henne, J. Hjorth, A. Hofzumahaus, H. Huntrieser, I. S. A. Isaksen, M. E. Jenkin, J. Kaiser, M. Kanakidou, Z. Klimont, M. Kulmala, P. Laj, M. G. Lawrence, J. D. Lee, C. Liousse, M. Maione, G. McFiggans, A. Metzger, A. Mieville,

- N. Moussiopoulos, J. J. Orlando, C. D. O'Dowd, P. I. Palmer, D. D. Parrish, A. Petzold, U. Platt, U. Pöschl, A. S. H. Prévôt, C. E. Reeves, S. Reimann, Y. Rudich, K. Sellegri, R. Steinbrecher, D. Simpson, H. ten Brink, J. Theloke, G. R. van der Werf, R. Vautard, V. Vestreng, Ch. Vlachokostas, R. von Glasow, *Atmos. Environ.* **43**(33), 5268 (2009).
- [3] K. Tørseth, W. Aas, K. Breivik, A. M. Fjæraa, M. Fiebig, A. G. Hjellbrekke, C. Lund Myhre, S. Solberg, K. E. Yttri, *Atmos. Chem. Phys.* **12**, 5447 (2012).
- [4] C. A. Brock, K. D. Froyd, M. Dollner, C. J. Williamson, G. Schill, D. M. Murphy, N. J. Wagner, A. Kupc, J. L. Jimenez, P. Campuzano-Jost, B. A. Nault, J. C. Schroder, D. A. Day, D. J. Price, B. Weinzierl, J. P. Schwarz, J. M. Katich, S. Wang, L. Zeng, R. Weber, J. Dibb, E. Scheuer, G. S. Diskin, J. P. DiGangi, T. Bui, J. M. Dean-Day, C. R. Thompson, J. Peischl, T. B. Ryerson, I. Bourgeois, B. C. Daube, R. Commane, S. C. Wofsy, *Atmos. Chem. Phys.* **21**, 15023 (2021).
- [5] G. Myhre, C. E. L. Myhre, B. H. Samset, T. Storelvmo, *Nat. Sci. Educ.* **4**(5), 7 (2013).
- [6] U. Pöschl, *Angew. Chem. Int. Ed. Engl.* **44**(46), 7520 (2005).
- [7] A. Brostrom, K. I. Kling, K. S. Hougaard, K. Molhave, *Sci. Rep.* **10**(1), 9150 (2020).
- [8] P. H. McMurry, *Ency. Atmos. Sci.* 20 (2003).
- [9] A. Virkkula, H. Grythe, J. Backman, T. Petaja, M. Busetto, C. Lanconelli, A. Lupi, S. Becagli, R. Traversi, M. Severi, V. Vitale, P. Sheridan, E. Andrews, *Atmos. Chem. Phys.* **22**(7), 5033 (2022).
- [10] M. Granados-Muñoz, J. L. Rascado, J. Bravo-Aranda, F. Guzmán, A. Gutiérrez, H. Lyamani, A. Chaikovsky, U. Wandinger, A. Ansmann, O. Dubovik, J. Grudo, L. Arboledas, *J. Geophys. Res. Atmos.* **119**, 4836 (2014).
- [11] V. Noel, D. M. Winker, M. McGill, P. Lawson, *J. Geophys. Res.* **109**, D24213 (2004).
- [12] M. Pahlow, D. Müller, M. Tesche, H. Eichler, G. Feingold, W. L. Eberhard, Y.-F. Cheng, *Appl. Opt.* **45**, 7429 (2006).
- [13] A. Nemuc, J. Vasilescu, C. Talianu, L. Belegante, D. Nicolae, *Atmos. Meas. Tech.* **6**(11), 3243 (2013).
- [14] L. Belegante, J. A. Bravo-Aranda, V. Freudenthaler, D. Nicolae, A. Nemuc, D. Ene, L. Alados-Arboledas, A. Amodeo, G. Pappalardo, G. D'Amico, F. Amato, R. Engelmann, H. Baars, U. Wandinger, A. Papayannis, P. Kokkalis, S. N. Pereira, *Atmos. Meas. Tech.* **11**(2), 1119 (2018).
- [15] Y. Gong, L. Bu, B. Yang, F. Mustafa, *Sensors* **20**, 2211 (2020).
- [16] E. W. Eloranta, *High Spectral Resolution Lidar, in Lidar: Range-Resolved Optical Remote Sensing of the Atmosphere*, pp. 143–163, Springer, New York (2005).
- [17] P. Rieger, A. Ullrich, *Proceedings of SPIE* **8186**, 81860A (2011).
- [18] U. Wandinger, *Optical Sciences* **102**, 241 (2005).
- [19] J. Bühl, P. Seifert, M. Radenz, H. Baars, A. Ansmann, *Atmos. Meas. Tech.* **12**(12), 6601 (2019).
- [20] G. Avdikos, *EPJ Web of Conferences* **89**, 04003 (2015).
- [21] D. Cholleton, P. Rairoux, A. Miffre, *Remote Sens.* **14**(15), 3767 (2022).
- [22] A. Miffre, D. Cholleton, T. Mehri, P. Rairoux, *Remote Sens.* **11**(15), 1761 (2019).
- [23] I. Veselovskii, A. Kolgotin, V. Griaznov, D. Müller, K. Franke, D. N. Whiteman, *Appl. Opt.* **43**(5), 1180 (2004).
- [24] G. Pappalardo, *EPJ Web of Conferences* **176**, 09004 (2018).
- [25] A. Comerón, C. Muñoz-Porcar, F. Rocadenbosch, A. Rodríguez-Gómez, M. Sicard, *Sensors (Basel)* **17**(6), 1450 (2017).
- [26] D. Nicolae, C. Talianu, *Atmospheric lidar and retrieval of aerosol optical characteristics, "Recent Advances in Atmospheric lidars"*, INOE Publishing House, Măgurele, 1-86 (2010).
- [27] V. Freudenthaler, H. Linné, A. Chaikovski, D. Rabus, S. Groß, *Atmos. Meas. Tech. Discuss.*, <https://doi.org/10.5194/amt-2017-395> (2018).
- [28] U. Wandinger, V. Freudenthaler, H. Baars, A. Amodeo, R. Engelmann, I. Mattis, S. Groß, G. Pappalardo, A. Giunta, G. D'Amico, A. Chaikovsky, F. Osipenko, A. Slesar, D. Nicolae, L. Belegante, C. Talianu, I. Serikov, H. Linné, F. Jansen, A. Apituley, K. M. Wilson, M. de Graaf, T. Trickl, H. Giehl, M. Adam, A. Comerón, C. Muñoz-Porcar, F. Rocadenbosch, M. Sicard, S. Tomás, D. Lange, D. Kumar, M. Pujadas, F. Molero, A. J. Fernández, L. Alados-Arboledas, J. A. Bravo-Aranda, F. Navas-Guzmán, J. L. Guerrero-Rascado, M. J. Granados-Muñoz, J. Preißler, F. Wagner, M. Gausa, I. Grigorov, D. Stoyanov, M. Iarlori, V. Rizi, N. Spinelli, A. Boselli, X. Wang, T. Lo Feudo, M. R. Perrone, F. De Tomasi, P. Burlizzi, *Atmos. Meas. Tech.* **9**(3), 1001 (2016).
- [29] V. Vakkari, H. Baars, S. Bohlmann, J. Bühl, M. Komppula, R.-E. Mamouri, E. J. O'Connor, *Atmos. Chem. Phys.* **21**(8), 5807 (2021).
- [30] A. Comerón, A. Rodríguez-Gómez, M. Sicard, R. Barragán, C. Muñoz-Porcar, F. Rocadenbosch, M. J. Granados-Muñoz, *Sensors (Basel)* **18**(6), 1807 (2018).
- [31] A. Behrendt, T. Nakamura, *Opt. Express* **10**(16), 805 (2002).
- [32] H. Adachi, T. Shibata, Y. Iwasaka, M. Fujiwara, *Appl. Opt.* **40**(36), 6587 (2001).
- [33] A. Behrendt, T. Nakamura, *Opt. Express* **10**(16), 805 (2002).
- [34] K. Sassen, *Bull. Amer. Meteor. Soc.* **72**(12), 1848 (1991).
- [35] C. M. R. Platt, *J. Appl. Meteorol.* **16**(4), 339 (1977).
- [36] J. L. Pezzaniti, R. A. Chipman, *Appl. Opt.* **33**(10), 1916 (1994).
- [37] J. M. Alvarez, M. A. Vaughan, C. A. Hostetler,

- W. H. Hunt, D. M. Winkler, *J. Atmos. Ocean. Technol.* **23**(5), 683 (2006).
- [38] V. Freudenthaler, *Atmos. Meas. Tech.* **9**(9), 4181 (2016).
- [39] J. A. Bravo-Aranda, L. Belegante, V. Freudenthaler, L. Alados-Arboledas, D. Nicolae, M. J. Granados-Muñoz, J. L. Guerrero-Rascado, A. Amodeo, G. D'Amico, R. Engelmann, G. Pappalardo, P. Kokkalis, R. Mamouri, A. Papayannis, F. Navas-Guzmán, F. J. Olmo, U. Wandinger, F. Amato, M. Haeffelin, *Atmos. Meas. Tech.* **9**(10), 4935 (2016).
- [40] I. Mattis, G. D'Amico, H. Baars, A. Amodeo, F. Madonna, M. Iarlori, *Atmos. Meas. Tech.* **9**(7), 3009 (2016).
- [41] G. D'Amico, A. Amodeo, I. Mattis, V. Freudenthaler, G. Pappalardo, *Atmos. Meas. Tech.* **9**(2), 491 (2016).
- [42] G. D'Amico, A. Amodeo, H. Baars, I. Biniotoglou, V. Freudenthaler, I. Mattis, U. Wandinger, G. Pappalardo, *Atmos. Meas. Tech.* **8**(11), 4891 (2015).
- [43] L. Belegante, D. Nicolae, A. Nemuc, C. Talianu, C. Derognat, *Acta Geophys.* **62**(2), 276 (2014).
- [44] D. Nicolae, J. Vasilescu, C. Talianu, I. Biniotoglou, A. V. Nicolae, S. Andrei, B. Antonescu, *Atmos. Chem. Phys.* **18**(19), 14511 (2018).
- [45] Y. Wan, Y. Chen, K. Li, *Journal of Cleaner Production*, **359**, 131959 (2022).

*Corresponding author: belegantelivio@inoe.ro